



Article

# Hydrogen Production through Catalytic Water Splitting Using Liquid-Phase Plasma over Bismuth Ferrite Catalyst

Kyong-Hwan Chung <sup>1</sup>, Hyun-Hak Jung <sup>1</sup>, Sun-Jae Kim <sup>2</sup> , Young-Kwon Park <sup>3</sup>, Sang-Chai Kim <sup>4</sup>  
and Sang-Chul Jung <sup>1,\*</sup>

<sup>1</sup> Department of Environmental Engineering, Suncheon National University, Suncheon 57922, Korea; likeu21@hanmail.net (K.-H.C.); brand7911@nate.com (H.-H.J.)

<sup>2</sup> Faculty of Nanotechnology and Advanced Materials Engineering, Sejong University, Seoul 05006, Korea; sjkim1@sejong.ac.kr

<sup>3</sup> School of Environmental Engineering, University of Seoul, Seoul 02504, Korea; catalica@uos.ac.kr

<sup>4</sup> Department of Environmental Education, Mokpo National University, Muan 58554, Korea; gikim@mokpo.ac.kr

\* Correspondence: jsc@sunchon.ac.kr; Tel.: +82-61-750-3814

**Abstract:** This study examined the H<sub>2</sub> production characteristics from a decomposition reaction using liquid-phase plasma with a bismuth ferrite catalyst. The catalyst was prepared using a sol-gel reaction method. The physicochemical and optical properties of bismuth ferrite were analyzed. H<sub>2</sub> production was carried out from a distilled water and aqueous methanol solution by direct irradiation via liquid-phase plasma. The catalyst absorbed visible-light over 610 nm. The measured bandgap of the bismuth ferrite was approximately 2.0 eV. The liquid-phase plasma emitted UV and visible-light simultaneously according to optical emission spectrometry. Bismuth ferrite induced a higher H<sub>2</sub> production rate than the TiO<sub>2</sub> photocatalyst because it responds to both UV and visible light generated from the liquid-phase plasma.

**Keywords:** H<sub>2</sub> production; water splitting; liquid-phase plasma; bismuth ferrite; optical emission



**Citation:** Chung, K.-H.; Jung, H.-H.; Kim, S.-J.; Park, Y.-K.; Kim, S.-C.; Jung, S.-C. Hydrogen Production through Catalytic Water Splitting Using Liquid-Phase Plasma over Bismuth Ferrite Catalyst. *Int. J. Mol. Sci.* **2021**, *22*, 13591. <https://doi.org/10.3390/ijms222413591>

Academic Editor: Albert Poater

Received: 15 November 2021

Accepted: 16 December 2021

Published: 18 December 2021

**Publisher's Note:** MDPI stays neutral with regard to jurisdictional claims in published maps and institutional affiliations.



**Copyright:** © 2021 by the authors. Licensee MDPI, Basel, Switzerland. This article is an open access article distributed under the terms and conditions of the Creative Commons Attribution (CC BY) license (<https://creativecommons.org/licenses/by/4.0/>).

## 1. Introduction

Recently, as climate change has become more serious, measures have been sought to suppress the use of fossil fuels, which is the main cause of climate change, and to reduce the amount of carbon dioxide. Hydrogen energy is attracting attention as a clean alternative energy source that does not cause carbon dioxide or pollution. Therefore, there is a growing interest in expanding the use of hydrogen energy and securing more efficient hydrogen energy production technology. So far, most hydrogen production has been obtained from petroleum-based petrochemical processes or from steam reforming of methane or propane [1,2]. However, since these methods use hydrocarbons as starting materials, they release warming gases, such as carbon dioxide. Therefore, research on a hydrogen production process that does not emit carbon dioxide is receiving increasingly more attention [3,4]. Among them, hydrogen production by water electrolysis or photocatalytic decomposition is a clean technology that does not emit carbon dioxide. In addition, it can be recognized as a method of producing clean hydrogen when the electrical energy used in the reaction is obtained from renewable energy [5]. On the other hand, this method has a limitation in that the hydrogen productivity is low [6,7]. Therefore, an environmentally friendly way to produce hydrogen in large quantities has become the focus of research.

Since the discovery of photochemical reactions in which TiO<sub>2</sub> electrodes decompose water to hydrogen and oxygen by photoelectrochemical reactions, various metal oxide photocatalysts have been developed [8–12]. TiO<sub>2</sub> is chemically stable and has been studied extensively for photocatalytic reactions among them [13]. On the other hand, the quantum efficiency of TiO<sub>2</sub> is limited by its wide bandgap and a high recombination rate of

electron–hole. Therefore, a visible-light-responsive photocatalyst is essential for developing eco-technology by hydrogen production and organic matter cracking using solar energy. Nevertheless, the development of visible-light-sensitive photocatalysts is still at the research level and remains a major challenge.

A photocatalyst with high photo-reactivity can be produced by doping the TiO<sub>2</sub> surface with metals or nonmetal ions, bonding to a semiconductor with a narrow bandgap, or doping with precious metals. Many studies have attempted to reform TiO<sub>2</sub> [14–16]. The method of doping nitrogen on the TiO<sub>2</sub> surface effectively reduces the bandgap by mixing the N 2*p* and O 2*p* states [17]. The photocatalyst efficiency was also shown to improve by doping the TiO<sub>2</sub> structure with transition metals. Doping the TiO<sub>2</sub> lattice with transition metals was shown to result in a red shift and enhance the photocatalytic activity [18]. The incorporation of the dopant increases or decreases the bandgap. The red-shift in the light absorption spectrum of Mn and N-doped TiO<sub>2</sub> results in the formation of new energy levels between the Ti 3*d* state in the conduction band and the O 2*p* state in the valence band, resulting in a decrease in the bandgap [19].

Bismuth ferrite (BF) has ferromagnetic, ferroelectric, and hyperelastic properties [20], and has attracted considerable attention due to its high performance as a sensor material, data storage materials, and photovoltaic cells [21,22]. BF is a type of perovskite with a high ABO<sub>3</sub> type and a multi-stiff material that exhibits both ferromagnetic and ferroelectric properties at room temperature [23]. Recently, it was reported that BF exhibits distinguish photo-catalytic activity in visible-light because of its narrow bandgap and high photovoltaic effects [24]. BF has a high response to visible light and is chemically stable. In addition, because BF nanocrystallines have magnetic semiconductor properties, they can be separated easily from solution [25]. In addition, the photovoltaic effects of BF also show increased reaction efficiency by inhibiting electron–hole recombination during the photochemical reaction [26]. Thus, BF is an interesting visible-light-sensitive photocatalyst that can be used for wastewater purification or H<sub>2</sub> production from water using sunlight [27,28]. A method to enhance the photocatalytic activity of BF by doping the BF structure with rare earth elements has been studied [29].

This study examined hydrogen production from the decomposition reaction using a liquid-phase plasma (LPP) on a BF catalyst. The BF was prepared using a sol–gel method. The structural properties of the BFs prepared by varying calcining temperatures were investigated. The physicochemical and optical properties of BF were also analyzed. Hydrogen production was carried out in distilled water and aqueous methanol solutions by direct irradiation of LPP. The hydrogen production abilities were measured in various photocatalysts, including BF, and the results were studied in connection with the optical emission properties of LPP and absorption properties of light of the photocatalysts.

## 2. Results and Discussion

### 2.1. Physicochemical Properties of BF Photocatalysts

Figure 1 presents the X-ray diffraction (XRD) patterns according to the heat treatment temperature of the BFs, which were heated at various temperatures. BiFeO<sub>3</sub>, Bi<sub>24</sub>Fe<sub>2</sub>O<sub>39</sub>, and Bi<sub>6</sub>O<sub>5</sub>(OH)<sub>3</sub>(NO<sub>3</sub>)<sub>5</sub>·2H<sub>2</sub>O structures were observed in the BF sample heat treated at 130 °C. BiFeO<sub>3</sub>, Bi<sub>24</sub>Fe<sub>2</sub>O<sub>39</sub> and Bi<sub>6</sub>O<sub>5</sub>(OH)<sub>3</sub>(NO<sub>3</sub>)<sub>5</sub>·2H<sub>2</sub>O structures were compared with reference to JCPDS data [30,31]. The JCPDS data of BiFeO<sub>3</sub>, Bi<sub>24</sub>Fe<sub>2</sub>O<sub>39</sub>, and Bi<sub>6</sub>O<sub>5</sub>(OH)<sub>3</sub>(NO<sub>3</sub>)<sub>5</sub>·2H<sub>2</sub>O structures are inserted in Figure 1. The standard XRD data of amorphous Bi<sub>24</sub>Fe<sub>2</sub>O<sub>39</sub> was referred to in the literature [32]. When the BF was heat-treated at 300 °C, BiFeO<sub>3</sub> and Bi<sub>6</sub>O<sub>5</sub>(OH)<sub>3</sub>(NO<sub>3</sub>)<sub>5</sub>·2H<sub>2</sub>O disappeared, and an amorphous Bi<sub>24</sub>Fe<sub>2</sub>O<sub>39</sub> material was mainly observed. When the BF was calcined at 500 °C, a small amount of the Bi<sub>24</sub>Fe<sub>2</sub>O<sub>39</sub> structure was observed, but it was mostly BiFeO<sub>3</sub>. When the BF was calcined at 600 °C, the peak representing the BiFeO<sub>3</sub> structure became shaper and showed an almost pure BiFeO<sub>3</sub> crystal structure.

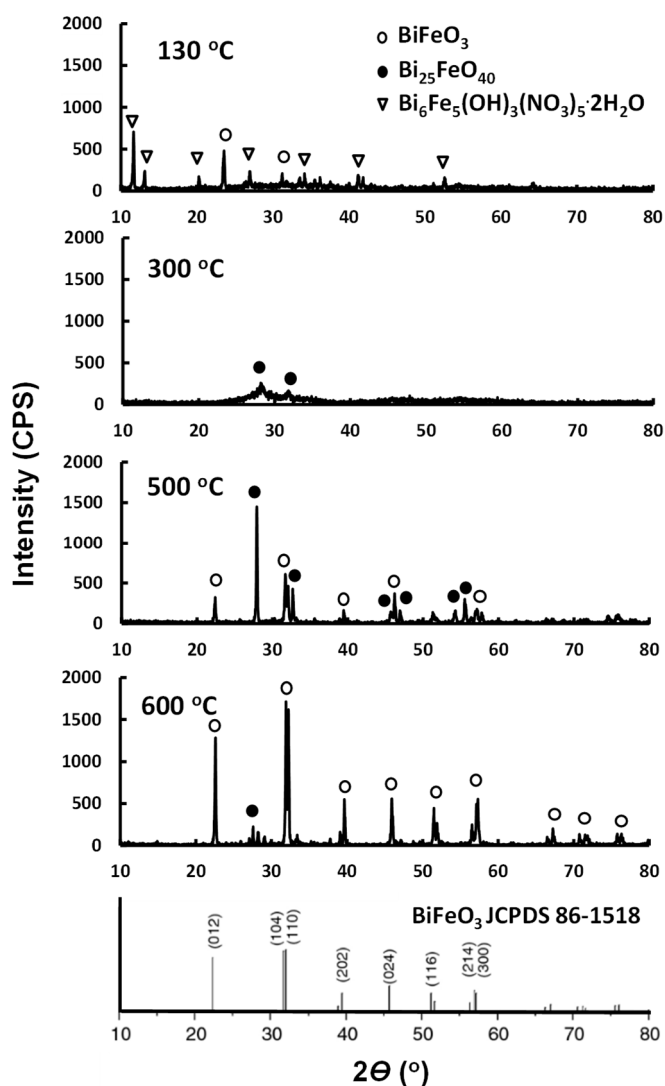


**Figure 1.** XRD patterns according to the heat treatment temperature.

Figure 1 shows the X-ray diffraction (XRD) patterns according to the annealing temperature of BF heated at various temperatures. In the BF sample annealed at 130 °C, the  $\text{Bi}_6\text{O}_5(\text{OH})_3(\text{NO}_3)_5 \cdot 2\text{H}_2\text{O}$  structure was mainly observed. The structures of  $\text{BiFeO}_3$  (JCPDS 86-1518),  $\text{Bi}_{25}\text{FeO}_{40}$  (JCPDS 46-0416), and  $\text{Bi}_6\text{O}_5(\text{OH})_3(\text{NO}_3)_5 \cdot 2\text{H}_2\text{O}$  (ICSD 2406) were compared with reference to JCPDS data [30,31]. The JCPDS data of the  $\text{BiFeO}_3$  structure are inset in Figure 1. Standard XRD data of amorphous  $\text{Bi}_{25}\text{FeO}_{40}$  were referenced in literature [32]. When BF was heat treated at 300 °C,  $\text{Bi}_6\text{O}_5(\text{OH})_3(\text{NO}_3)_5 \cdot 2\text{H}_2\text{O}$  disappeared and amorphous  $\text{Bi}_{25}\text{FeO}_{40}$  material was mainly observed. The intensity of the XRD peak was very low. When BF was calcined at 500 °C, a  $\text{Bi}_{25}\text{FeO}_{40}$  peak and a  $\text{BiFeO}_3$  peak were mixed. When BF was calcined at 600 °C, the  $\text{BiFeO}_3$  structure was predominant, and the  $\text{Bi}_{25}\text{FeO}_{40}$  peak was significantly reduced. It exhibits an almost pure  $\text{BiFeO}_3$  crystal structure.

Figure 2a presents scanning electron microscopy (SEM) images and energy-dispersive X-ray spectroscopy (EDS) results of BF. Figure 2b presents transmission electron microscope (TEM) image of BF. The BF crystals showed irregular polygonal structures in the image. The size of the BF particles in the image was measured to be about 60 nm from TEM image. The particles appeared to be agglomerated with each other. The shape and size of the particles were similar regardless of the calcining temperature. The EDS revealed the two BFs to have similar components. The peaks for Fe were also observed in both EDS results. Figure 2c illustrates the FT-IR spectra of BF nanoparticles. The  $594\text{ cm}^{-1}$  and  $457\text{ cm}^{-1}$  peaks in the samples were assigned to the mode of stretching vibrations along

the Fe-O axis and the mode of the Fe-O bending vibration, respectively [33]. This is the characteristic band exhibited by the  $\text{FeO}_6$  octahedron structure in the frame structure of the framework of perovskite [34]. The band at approximately  $1070\text{ cm}^{-1}$  was ascribed to the Bi-O bonds vibration [35]. The broadband in the  $3000\text{--}3500\text{ cm}^{-1}$  range was attributed to the symmetrical and asymmetric stretching vibrations of the  $\text{H}_2\text{O}$  and OH bond groups, and the band of  $1570\text{--}1600\text{ cm}^{-1}$  represents to the vibration of  $\text{H}_2\text{O}$  bending [36]. The peak at  $1380\text{--}1400\text{ cm}^{-1}$  was assigned to trace nitrates ( $\text{NO}_3^-$ ) [37]. The band at  $1574\text{ cm}^{-1}$  represents the H-O-H bending vibration. The peak at  $2965\text{ cm}^{-1}$  is attributed to the asymmetric stretching of  $\text{CH}_2$  and the peak appearing at  $3024\text{ cm}^{-1}$  is assigned to the symmetric stretching of  $\text{CH}_2$  [38].

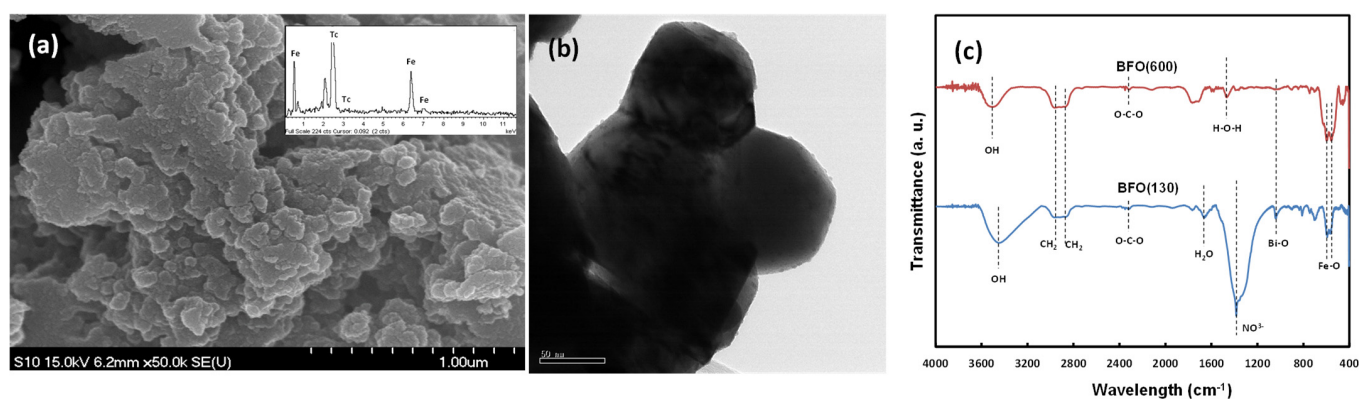


**Figure 2.** (a) SEM image with EDS results, (b) TEM image, and (c) FT-IR spectra of BF.

X-ray photoelectron spectroscopy (XPS) was performed to confirm the surface state of the synthesized BF nanoparticles. Figure 3 illustrates the entire XPS spectra of the BF photocatalyst. The peaks for BF, such as Bi  $4f_7$ , Bi  $4f_5$ , Fe  $2p_1$ , C  $1s$ , Fe  $2p_3$ , and O  $1s$  were observed. The C  $1s$  peak was also observed in the entire spectra, but the C adsorbed on the BF surface does not influence the physicochemical properties of the composites [39].

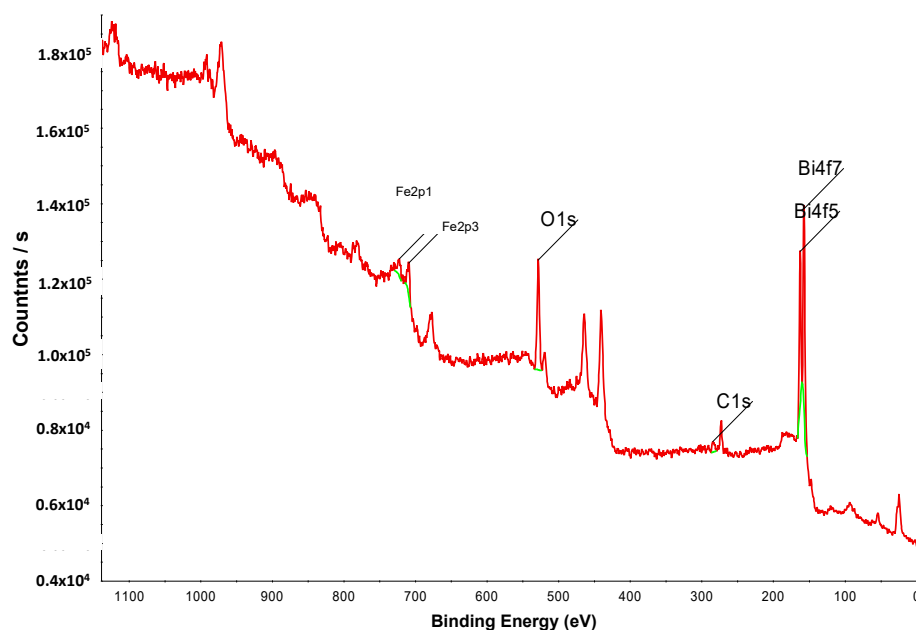


**Figure 3.** The entire XPS spectrum of BF.

Figure 4 presents the XPS spectra of Bi, Fe, and O for BF. The individual spectrum of the Fe 2*p* core level was measured. The characteristic peaks of Fe 2*p*<sub>1/2</sub> and Fe 2*p*<sub>3/2</sub> appeared at 710.6 eV and 724.7 eV binding energies, respectively. This suggests that the Fe in the BF is in the Fe<sup>3+</sup> state [40]. A weak satellite peak was obtained at 720 eV, indicating iron in the trivalent oxidation state and BF is BiFeO<sub>3</sub> [41]. The peak near 530 eV in the O 1*s* spectrum was assigned to the oxygen interacting with Fe<sup>3+</sup>. The peaks of Bi were observed in the Bi element spectra. In the XPS results, the strong peaks of the spectra at 164 eV and 159 eV for Bi<sup>3+</sup> were the Bi 4*f*<sub>5/2</sub> and Bi 4*f*<sub>7/2</sub> peaks [42]. The O 1*s* peak in the spectrum showed two kinds of chemical states of oxygen presents on BF. In the results, the peak at 529.3 eV binding energy was attributed to oxygen placed in the lattice, and the peak (~531.4 eV) corresponded to oxygen chemisorbed on the surface. The last peak was because BiFeO<sub>3</sub>-based compounds adsorb oxygen in the vacancies produced on the surface due to lattice defects [40].

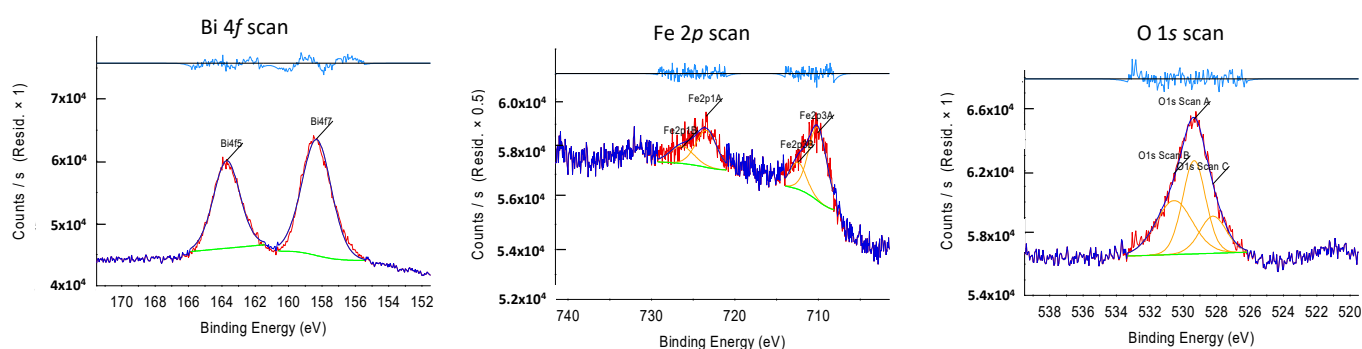


Figure 4. XPS spectra of Fe, Bi, and O for BF.

Figure 5a shows a plot of the Kubelka–Munk function converted from UV-visible DRS of the BF [43]. BF absorbed ultraviolet and visible ray up to approximately 610 nm. The bandgaps of the BFs are determined from the plot of the Kubelka–Munk function  $(F(R))^{1/2}$ , as shown in Figure 5b. The bandgap of BF photocatalyst was approximately 2.0 eV. The narrow bandgap of BF suggests that it can act photo-catalytic reaction, even in the visible-light region.

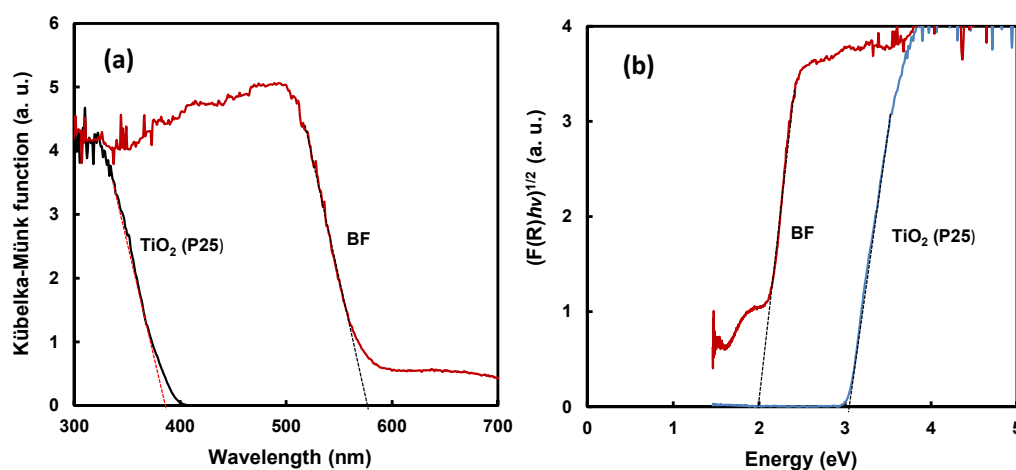


Figure 5. (a) Plot of the Kubelka–Munk function converted from UV-visible DRS and (b) relationship of  $(F(R)hv)^{1/2}$  versus energy.

## 2.2. H<sub>2</sub> production by the Photocatalytic Decomposition Using LPP

Figure 6a shows the optical emission spectroscopy (OES) spectrum of DW. The OES of DW by LPP irradiation showed peaks at 309 nm, 486 nm, 656 nm, 777 nm, and 844 nm.

Among the main peaks, the strongest peak appeared at 309 nm, which was an emission peak that appears along with the generation of OH radicals and shows strong oxidizing power [44]. In addition, it shows a strong emission peak at 656 nm. This emission peak appears along with H<sub>2</sub> generation and is an emission peak that appears when active species decompose water to generate H<sub>2</sub>. The emission peak at 486 nm also appeared along with H<sub>2</sub> production. The peaks at 777 nm and 844 nm were emission peaks appearing with oxygen production. On the other hand, the optical light emission by the LPP discharge in DW emits 309 nm-oriented UV light and visible-light of various wavelengths. Figure 6b shows the H<sub>2</sub> evolution rate (HER) under conditions without and with various catalysts in H<sub>2</sub> production from DW by LPP irradiation. H<sub>2</sub> was generated by the cracking of water, even in the absence of a catalyst. As confirmed in the OES, the light at 486 nm and 656 nm was emitted by the LPP discharge to generate hydrogen. The HER was increased using a photocatalyst, such as TiO<sub>2</sub>. The HER was high in the order of BF > Ni/TiO<sub>2</sub> > TiO<sub>2</sub>, which is related to the light absorption properties of the photocatalysts. According to the DRS results of each photocatalyst, TiO<sub>2</sub> showed light absorption ability only up to UV light, but the light absorption band of Ni/TiO<sub>2</sub> was expanded to the visible-ray region. The absorption region of BF was extended further into the visible-ray region. Therefore, in the Ni/TiO<sub>2</sub> photocatalyst, a photoreaction occurred due to more light absorption than TiO<sub>2</sub>, increasing the HER. The HER was increased greatly because it can cause photochemical reactions by absorbing visible-light in a wider wavelength band than BF.

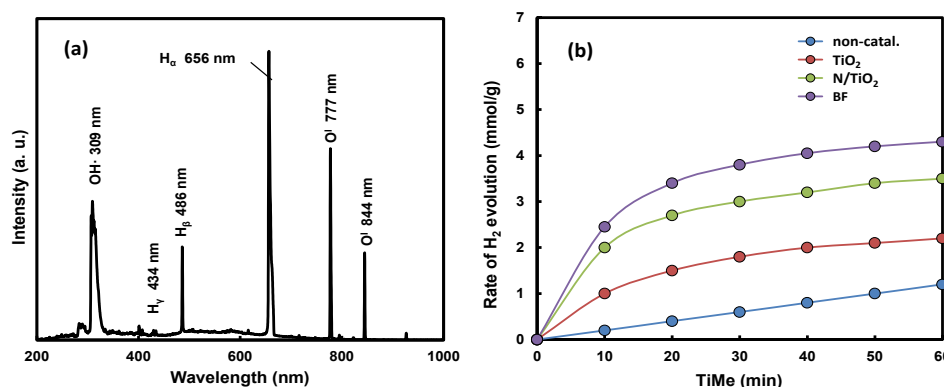


Figure 6. (a) OES spectrum of DW, and (b) HER under conditions without and with various catalysts.

Figure 7a illustrates the OES spectra by LPP discharge in an aqueous methanol solution with different concentrations. In the OES for an aqueous methanol solution, the optical emission peak at each wavelength was larger than the optical emission peak in DW. In particular, the optical emission peak of the wavelength in the UV region increased significantly. The OES spectra were studied in aqueous methanol solutions with different concentrations. The optical emission peak in the UV region increased gradually with increasing concentration but was highest when the methanol content was 10%. The emission peak decreased at higher concentrations. The size of the H<sup>α</sup> (656 nm) peak was the same regardless of the methanol concentration. The size of the H<sup>β</sup> peak at 486 nm slightly increased as the methanol concentration was increased. Figure 7b shows HER by the LPP irradiation and BF photocatalyst in an aqueous methanol solution with different concentrations. HER in the methanol solution was significantly higher than in DW. The highest HER was observed in a 10% aqueous methanol solution. The HER decreased gradually when the methanol concentration was higher than 10%. This is related to the change in OES according to the concentration of the aqueous methanol solution because UV emission is highest in an aqueous solution containing 10% methanol and decreases with increasing concentration. UV light emission was large in a 10% aqueous solution of methanol. Therefore, the photocatalytic decomposition of methanol and water occurred

most actively, which explains why the HER was higher than in aqueous methanol at different concentrations.

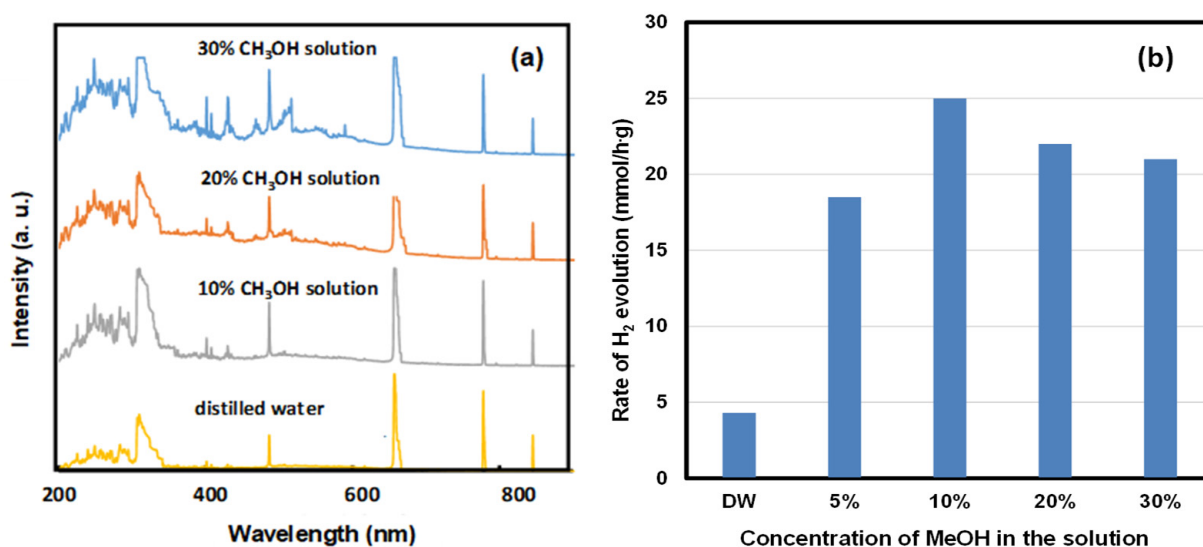


Figure 7. (a) OES spectra by LPP discharge and (b) HER of BF in an aqueous methanol solution with different concentrations.

### 3. Materials and Methods

#### 3.1. Preparation of BF Nanoparticle Photocatalyst

The BF nanoparticles were prepared by a sol–gel reaction. The reagents were 0.05 M Bi(NO<sub>3</sub>)<sub>3</sub>·5H<sub>2</sub>O (Daejung, Gyeonggi-do, Korea, 99.5%), 0.05 M iron nitrate (Fe(NO<sub>3</sub>)<sub>3</sub>·9H<sub>2</sub>O; (Daejung, Gyeonggi-do, Korea, 99.5%), and 4.3 M C<sub>2</sub>H<sub>5</sub>OH (Daejung, Gyeonggi-do, Korea, 98%). The mixture of the reagents was stirred at 70 °C for 3 h to prepare a BF sol. The sol was dried at 150 °C for 1 day to prepare a powder, which was heated at 300 °C for 3 h and calcined at 600 °C for 4 h to get a BF powder. Commercial TiO<sub>2</sub> (Evonik Degussa, Essen, Germany, P25) was applied as the control catalyst, Ni/TiO<sub>2</sub> was prepared by doping Ni ions on TiO<sub>2</sub> prepared using the sol–gel method [45].

#### 3.2. Catalytic water Splitting Using LPP

Figure 8 shows a schematic diagram of a reactor for producing hydrogen by applying an LPP system. A catalyst (0.5 g) was injected into 100 mL of distilled water (DW) and reacted. The LPP reaction was carried out in a liquid mixed with the catalyst. The internal temperature of the reactor was maintained at 15 °C using a thermostatic circulator (Daehan, S2050, Seoul, Korea). The flow rate of hydrogen generated during the reaction was measured using a mass flow meter for measuring H<sub>2</sub> gas (MFC Korea, TS-D2500, Buchon, Korea). The composition of the generated gas was analyzed by GC (Younglin, M700D, Anyang, Korea). Plasma was generated by the pulse discharge between the electrode and the electrode by the plasma generator [46]. Tungsten rods (D = 6 mm) were used as electrodes. The range of the plasma pulse width was 2–6 μs, and the frequency range of the plasma was adjusted to 20–35 kHz.

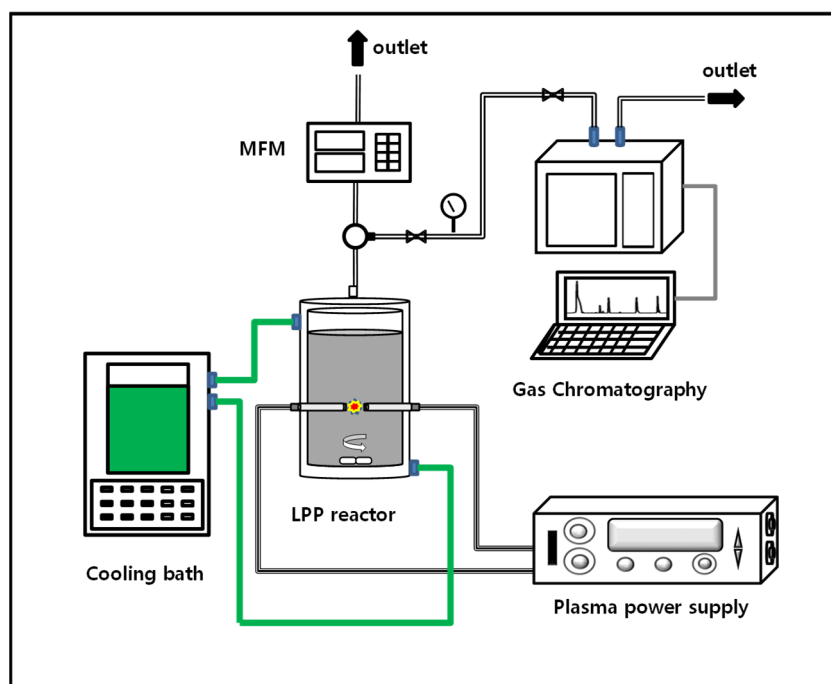


**Figure 8.** Schematic diagram of a photocatalytic reaction device using the LPP system.

### 3.3. Characterization of BF Photocatalysts and Optical Emission of the LPP

The crystallinity and structure of the BF were observed by XRD system (Rigaku, D/Maxi Ultima III, Tokyo, Japan) using a  $\text{CuK}\alpha$  X-ray radiation with Ni-filtered ( $\lambda = 1.5405 \text{ \AA}$ ). The morphology and crystal size of the BF were surveyed by SEM system (Hitachi, S-4900/EXE-3000, Tokyo, Japan). The chemical compositions of the BF were surveyed by EDS system (NORANSE Z-MAX 550, Tokyo, Japan). FT-IR spectroscopy (Shimadzu, IRP resitge-21, Tokyo, Japan) of BF was performed to measure the functional groups. The binding state of the BF elements was investigated by XPS system (VG System, Multi-Lab 1000, East Grinstead, UK). Al  $\text{K}\alpha$  X-rays were used to measure the chamber at  $10^{-6}$ – $10^{-7}$  Pa. The light absorption characteristics of the BF were analyzed by ultraviolet-visible DRS system (Shimadzu, UV-2750, Tokyo, Japan) using  $\text{BaSO}_4$  as a reflective standard to acquire the DRS band of the BF at 200–1000 nm. The optical bandgap of the BF was determined using the Kubelka–Munk theory [43].

The OES of the LPP was performed while the plasma was directly irradiating the reactants using a fiber optic spectrometer (Avante, AvanSpec-4500, Louisville, KY, USA). The OES spectra were gathered by placing an optical fiber perpendicular to the axis of the needle electrode [47]. The measurement conditions for gathering the spectrum were 3  $\mu\text{s}$  pulse-width, 230 V discharge-voltage, and 35 kHz frequency.

## 4. Conclusions

The characteristics of  $\text{H}_2$  production by the catalyst of BF were studied in the cracking of water to which LPP was applied. BF absorbed visible-light over 610 nm. The bandgap of the BF photocatalyst was approximately 2.0 eV. LPP emitted ultraviolet and visible-light simultaneously. BF showed a higher  $\text{H}_2$  production rate than the  $\text{TiO}_2$  photocatalyst, which only absorbs ultraviolet light.

The HER was highest in the order of  $\text{BF} > \text{Ni/TiO}_2 > \text{TiO}_2$ . This is related to the light absorption properties of the photocatalyst. Although  $\text{TiO}_2$  showed light absorption only up to UV light, the light absorption band of  $\text{Ni/TiO}_2$  was expanded to the visible-ray region. The absorption range of BF was extended to the visible-ray region. The HER increased significantly because BF can cause a photochemical reaction by absorbing visible-light over a wider wavelength band.



In a methanol solution, the HER occurred at a significantly higher rate than in DW. The highest HER was observed in a 10% aqueous methanol solution. The HER decreased gradually when the methanol concentration was greater than 10% because UV emission was highest in the aqueous solution containing 10% methanol and decreased with increasing methanol concentration. Moreover, the photocatalytic decomposition of methanol and water occurred most actively in the 10% aqueous methanol solution because of the large UV light emission.

**Author Contributions:** K.-H.C. designed and performed the experiment. H.-H.J. and S.-J.K. contributed to the analysis and the interpretation of data. Y.-K.P. and S.-C.K. edited the original drafted paper. S.-C.J. supervised the experiments and paper. All authors have read and agreed to the published version of the manuscript.

**Funding:** This research was supported by the program of Future Hydrogen Original Technology Development (NRF-2021M3I3A1084797), through the National Research Foundation of Korea (NRF), funded by the Korean government (Ministry of Science and ICT(MSIT)).

**Institutional Review Board Statement:** Not applicable.

**Informed Consent Statement:** Not applicable.

**Data Availability Statement:** Not applicable.

**Conflicts of Interest:** The authors declare no conflict of interest.

## References

1. Pulido, M.E.; González, D.O.; Ortega, M.A.; López, C.R.; Nereida, S.M.; Doña, R.J.M.; Navío, J.A.; Fernández, H.D.; Pérez, P.J. Efficient and affordable hydrogen production by water photo-splitting using TiO<sub>2</sub>-based photocatalysts. *Int. J. Hydrog. Energy* **2013**, *38*, 2144–2152. [[CrossRef](#)]
2. Al-Mazroai, L.S.; Bowker, M.; Davies, P.; Dickinson, A.; Greaves, J.; James, D.; Millard, L. The photocatalytic reforming of methanol. *Catal. Today* **2007**, *122*, 46–50. [[CrossRef](#)]
3. Kirste, K.G.; McAulay, K.; Bell, T.E.; Stoian, D.; Laassiri, S.; Daisley, A.; Hargreaves, J.S.J.; Mathisen, K.; Torrente-Murciano, L. Co<sub>x</sub>-free hydrogen production from ammonia-mimicking the activity of Ru catalysts with unsupported Co-Re alloys. *Appl. Catal. B Environ.* **2021**, *280*, 119405. [[CrossRef](#)]
4. Zamfirescu, C.; Dincer, I. Ammonia as a green fuel and hydrogen source for vehicular applications. *Fuel Process. Technol.* **2009**, *90*, 729–737. [[CrossRef](#)]
5. Lam, S.S.; Liew, R.K.; Cheng, C.K.; Chase, H.A. Catalytic microwave pyrolysis of waste engine oil using metallic pyrolysis char. *Appl. Catal. B Environ.* **2015**, *176–177*, 601–617. [[CrossRef](#)]
6. Chiarello, G.L.; Myriam, H.; Aguire, E.S. Hydrogen production by photocatalytic steam reforming of methanol on noble metal-modified TiO<sub>2</sub>. *J. Catal.* **2010**, *273*, 182–190. [[CrossRef](#)]
7. Ahmad, H.; Kamarudin, S.K.; Minggu, L.J.; Kassim, M. Hydrogen from photocatalytic water splitting process: A review. *Renew. Sustain. Energy Rev.* **2015**, *43*, 599–610. [[CrossRef](#)]
8. Fujishima, A.; Honda, K. Electrochemical photolysis of water at a semiconductor electrode. *Nature* **2015**, *238*, 37–38. [[CrossRef](#)] [[PubMed](#)]
9. Yang, X.Y.; Wolcott, A.; Wang, G.M.; Sobo, A.; Fitzmorris, R.C.; Qian, F.; Zhang, J.Z.; Li, Y. Nitrogen-doped ZnO nanowire arrays for photoelectrochemical water splitting. *Nano Lett.* **2009**, *9*, 2331–2336. [[CrossRef](#)]
10. Wolcott, A.; Smith, W.A.; Kuykendall, T.R.; Zhao, Y.P.; Zhang, J.Z. Photoelectrochemical study of nanostructured ZnO thin films for hydrogen generation from water splitting. *Adv. Funct. Mater.* **2009**, *19*, 1849–1856. [[CrossRef](#)]
11. Zhang, Z.; Hossain, N.F.; Takahashi, T. Self-assembled hematite ( $\alpha$ -Fe<sub>2</sub>O<sub>3</sub>) nanotube arrays for photoelectrocatalytic degradation of azo dye under simulated solar light irradiation. *Appl. Catal. B Environ.* **2010**, *95*, 423–429. [[CrossRef](#)]
12. Weinhardt, L.; Blum, M.; Bar, M.; Heske, C.; Cole, B.; Marsen, B.; Miller, E.L. Electronic surface level positions of WO<sub>3</sub> thin films for photoelectrochemical hydrogen production. *J. Phys. Chem. C* **2008**, *112*, 3078–3082. [[CrossRef](#)]
13. Wu, H.; Zhang, Z. High photoelectrochemical water splitting performance on nitrogen doped double-wall TiO<sub>2</sub> nanotube array electrodes. *Int. J. Hydrog. Energy* **2011**, *36*, 13481–13487. [[CrossRef](#)]
14. Tian, J.; Leng, Y.; Zhao, Z.; Xia, Y.; Sang, Y.; Hao, P.; Zhan, J.; Li, M.; Liu, H. Carbon quantum dots/hydrogenated TiO<sub>2</sub> nanobelt heterostructures and their broad spectrum photocatalytic properties under UV, visible, and near-infrared irradiation. *Nano Energy* **2015**, *11*, 419–427. [[CrossRef](#)]
15. Sharotri, N.; Sud, D. Ultrasound-assisted synthesis and characterization of visible light responsive nitrogen-doped TiO<sub>2</sub> nanomaterials for removal of 2-chlorophenol. *Desalin. Water Treat.* **2016**, *57*, 8776–8788. [[CrossRef](#)]
16. Zhang, L.; Jing, D.; She, X.; Liu, H.; Yang, D.; Lu, Y.; Li, J.; Zheng, Z.; Guo, L. Heterojunctions in g-C<sub>3</sub>N<sub>4</sub>/TiO<sub>2</sub>(B) nanofibers with exposed (001) plane and enhanced visible-light photoactivity. *J. Mater. Chem. A* **2014**, *2*, 2071–2078. [[CrossRef](#)]

17. Asahi, R.; Morikawa, T.; Ohwaki, T.; Aoki, K.; Taga, Y. Visible-light photocatalysis in nitrogen-doped titanium oxides. *Science* **2001**, *293*, 269–271. [[CrossRef](#)]
18. Yamashita, H.; Harada, M.; Misaka, J.; Takeuchi, M.; Ikeue, K.; Anpo, M. Degradation of propanol diluted in water under visible light irradiation using metal ion-implanted titanium dioxide photocatalysts. *J. Photochem. Photobiol. A Chem.* **2002**, *148*, 257–261. [[CrossRef](#)]
19. Jedsukontorn, T.; Ueno, T.; Saito, N.; Hunsom, M. Narrowing bandgap energy of defective black TiO<sub>2</sub> fabricated by solution plasma process and its photocatalytic activity on glycerol transformation. *J. Alloys Compd.* **2018**, *757*, 188–199. [[CrossRef](#)]
20. Martin, L.W.; Crane, S.P.; Chu, Y.H.; Holcomb, M.B.; Gajek, M.; Huijben, M.; Yang, C.H.; Balke, N.; Ramesh, R. Multiferroics and magnetoelectrics: Thin films and nanostructures. *J. Phys. Condens. Matter.* **2008**, *20*, 434220–434233. [[CrossRef](#)]
21. Yi, H.T.; Choi, T.; Choi, S.G.; Oh, Y.S.; Cheong, S.W. Mechanism of the switchable photovoltaic effect in ferroelectric BiFeO<sub>3</sub>. *Adv. Mater.* **2011**, *23*, 3403–3407. [[CrossRef](#)] [[PubMed](#)]
22. Ji, W.; Yao, K.; Liang, Y.C. Bulk photovoltaic effect at visible wavelength in epitaxial ferroelectric BiFeO<sub>3</sub> thin films. *Adv. Mater.* **2010**, *22*, 1763–1766. [[CrossRef](#)]
23. Catalan, G.; Scott, J.F. Physics and applications of bismuth ferrite. *Adv. Mater.* **2009**, *21*, 2463–2485. [[CrossRef](#)]
24. Yang, S.Y.; Martin, L.W.; Byrnes, S.J.; Conry, T.E.; Basu, S.R.; Paran, D.; Reichertz, L.; Ihlefeld, J.; Adamo, C.; Melville, A.; et al. Photovoltaic effects in BiFeO<sub>3</sub>. *Appl. Phys. Lett.* **2009**, *95*, 062909. [[CrossRef](#)]
25. Li, S.; Lin, Y.H.; Zhang, B.P.; Wang, Y.; Nan, C.W. Controlled fabrication of BiFeO<sub>3</sub> uniform microcrystals and their magnetic and photocatalytic behaviors. *J. Phys. Chem. C* **2010**, *114*, 2903–2908. [[CrossRef](#)]
26. Ichiki, M.; Morikawa, Y.; Nakada, T. Electrical properties of ferroelectric lead lanthanum zirconate titanate as an energy transducer for application to electrostatic-optical motor. *Jpn. J. Appl. Phys.* **2002**, *41*, 6993–6996. [[CrossRef](#)]
27. Qin, M.; Yao, K.; Liang, Y.C.; Shannigrahi, S. Thickness effects on photoinduced current in ferroelectric Pb<sub>0.97</sub>La<sub>0.03</sub>Zr<sub>0.52</sub>Ti<sub>0.48</sub>O<sub>3</sub> thin films. *J. Appl. Phys.* **2007**, *104*, 014104–014108. [[CrossRef](#)]
28. Gao, F.; Chen, X.Y.; Yin, K.B.; Dong, S.; Ren, Z.F.; Yuan, F.; Yu, T.; Zou, Z.G.; Liu, J.M. Visible-light photocatalytic properties of weak magnetic BiFeO<sub>3</sub> nanoparticles. *Adv. Mater.* **2007**, *19*, 2889–2892. [[CrossRef](#)]
29. Guo, R.; Fang, L.; Dong, W.; Zheng, F.; Shen, M. Enhanced photocatalytic activity and ferromagnetism in Gd doped BiFeO<sub>3</sub> nanoparticles. *J. Phys. Chem. C* **2010**, *114*, 21390–213906. [[CrossRef](#)]
30. Azmy, H.A.M.; Razuki, N.A.; Aziz, A.W.; Satar, N.S.A.; Kaus, N.H.M. Visible light photocatalytic activity of BiFeO<sub>3</sub> nanoparticles for degradation of methylene blue. *J. Phys. Sci.* **2017**, *28*, 85–103. [[CrossRef](#)]
31. Pang, J.; Han, Q.; Liu, W.; Shen, Z.; Wang, X.; Zhu, J. Two basic bismuth nitrates: [Bi<sub>6</sub>O<sub>6</sub>(OH)<sub>2</sub>](NO<sub>3</sub>)<sub>4</sub>·2H<sub>2</sub>O with superior photodegradation activity for rhodamine B and [Bi<sub>6</sub>O<sub>5</sub>(OH)<sub>3</sub>](NO<sub>3</sub>)<sub>5</sub>·3H<sub>2</sub>O with ultrahigh adsorption capacity for methyl orange. *Appl. Surf. Sci.* **2017**, *422*, 283–294. [[CrossRef](#)]
32. Yang, X.; Xu, G.; Ren, Z.; Wei, X.; Chao, C.; Gong, S.; Shen, G.; Han, G. The hydrothermal synthesis and formation mechanism of single-crystalline perovskite BiFeO<sub>3</sub> microplates with dominant (012) facets. *Cryst. Eng. Comm.* **2014**, *16*, 4176–4182. [[CrossRef](#)]
33. Bhalodia, J.A.; Kanjariya, P.V.; Mankadia, S.R.; Jadav, G.D. Structural and magnetic characterization of BiFeO<sub>3</sub> nano-particles synthesized using auto-combustion technique. *Int. J. Chem. Tech. Res.* **2014**, *6*, 2144–2146.
34. Vijayasundaram, S.V.; Kanagadurai, R. Size dependent magnetic properties of BiFeO<sub>3</sub> nanoparticles: A multifunctional material for saving energy. *Int. J. Chem. Tech. Res.* **2015**, *8*, 436–440.
35. Chaturvedi, S.C.; Shirolkar, M.M.; Rajendra, R.; Singh, S.; Ballav, N.; Kulkarni, S. Coercivity and exchange bias of bismuth ferrite nanoparticles isolated by polymer coating. *J. Appl. Phys.* **2014**, *115*, 123906. [[CrossRef](#)]
36. Rao, G.V.S.; Rao, C.N.R.; Ferraro, J.R. Infrared and electronic spectra of rare earth perovskites: Ortho-chromites, -manganites and -ferrites. *Appl. Spectrosc.* **1970**, *24*, 436–445. [[CrossRef](#)]
37. Hua, K.; Wang, W.; Wang, Y.; Xu, J.; Jia, D.; Lu, Z.; Zhou, Y. Factors controlling pure-phase multiferroic BiFeO<sub>3</sub> powders synthesized by chemical co-precipitation. *J. Alloys Compd.* **2011**, *509*, 2192–2197.
38. Dash, S.; Choudhary, R.N.P.; Goswami, M.N. Enhanced dielectric and ferroelectric properties of PVDF-BiFeO<sub>3</sub> composites in 0e3 connectivity. *J. Alloys Compd.* **2017**, *715*, 29–35. [[CrossRef](#)]
39. Wang, X.; Lin, Y.; Ding, X.F.; Jiang, J.G. Enhanced visible-light-response photocatalytic activity of bismuth ferrite nanoparticles. *J. Alloys Compd.* **2011**, *509*, 6585–6588. [[CrossRef](#)]
40. Gao, T.; Chen, Z.; Zhu, Y.; Niu, F.; Huanh, Q.; Qin, L.; Sun, X.; Huang, Y. Synthesis of BiFeO<sub>3</sub> nanoparticles for the visible-light induced photocatalytic property. *Mater. Res. Bull.* **2014**, *59*, 6–12. [[CrossRef](#)]
41. García-Zaldívar, O.; Díaz-Castañón, S.; Espinoza-Beltrán, F.J.; Hernández-Landaverde, M.A.; López, Z.; Faloh-Gandarilla, J.; Calderón-Piñar, F. BiFeO<sub>3</sub> codoping with Ba, La and Ti: Magnetic and structural studies. *J. Adv. Dielectr.* **2015**, *5*, 1550034. [[CrossRef](#)]
42. Lijing, D.; Yang, H.; Xian, T.; Chen, X. Enhanced Photocatalytic Activity of NaBH<sub>4</sub> Reduced BiFeO<sub>3</sub> Nanoparticles for Rhodamine B Decolorization. *Materials* **2017**, *10*, 1118.
43. Kübelka, P.; Münk, F. Ein Beitrag zur optik der farbanstriche. *Zeitschrift für Physik* **1931**, *12*, 593–596.
44. Park, Y.K.; Kim, B.J.; Jeong, S.; Jeon, K.J.; Chung, K.H.; Jung, S.C. Characteristics of hydrogen production by photocatalytic waster splitting using liquid phase plasma over Ag-doped TiO<sub>2</sub> photocatalysts. *Environ. Res.* **2020**, *188*, 109630. [[CrossRef](#)] [[PubMed](#)]
45. Chung, K.H.; Park, H.; Jeon, K.J.; Park, Y.K.; Jung, S.C. Irradiation of liquid phase plasma on photocatalytic decomposition of acetic acid-containing wastewater over metal oxide photocatalysts. *Catal. Today* **2018**, *307*, 131–139. [[CrossRef](#)]

- 
46. Kim, S.C.; Park, Y.K.; Jung, S.C. Recent applications of the liquid phase plasma process. *Korean J. Chem. Eng.* **2021**, *38*, 885–898. [[CrossRef](#)]
  47. Jeong, S.; Chung, K.H.; Lee, H.; Park, H.; Jeon, K.J.; Park, Y.K.; Jung, S.C. Enhancement of hydrogen evolution from water photocatalysis using liquid phase plasma on metal oxide-loaded photocatalysts. *ACS Sustain. Chem. Eng.* **2017**, *5*, 3659–3666. [[CrossRef](#)]